

## Research Article

Karupiah Senthilvadivu, Karuppusamy Loganathan\*, Mohamed Abbas, and Mohammed S. Alqahtani

# Numerical study of blood-based MHD tangent hyperbolic hybrid nanofluid flow over a permeable stretching sheet with variable thermal conductivity and cross-diffusion

<https://doi.org/10.1515/phys-2024-0018>  
received June 05, 2023; accepted April 08, 2024

**Abstract:** Modern heat transport processes such as fuel cells, hybrid engines, microelectronics, refrigerators, heat exchangers, grinding, coolers, machining, and pharmaceutical operations may benefit from the unique properties of nanoliquids. By considering  $\text{Al}_2\text{O}_3$  nanoparticles as a solo model and  $\text{Al}_2\text{O}_3\text{-Cu}$  as hybrid nanocomposites in a hyperbolic tangent fluid, numerical simulations for heat and mass transfer have been established. To compare the thermal acts of the nanofluid and hybrid nanofluid, bvp4c computes the solution for the created mathematical equations with the help of MATLAB software. The impacts of thermal radiation, such as altering thermal conductivity and cross-diffusion, as well as flow and thermal facts, including a stretchy surface with hydromagnetic, and Joule heating, were also included. Furthermore, the hybrid nanofluid generates heat faster than a nanofluid. The temperature and concentration profiles increase with the Dufour and the Soret numbers, respectively. The upsurge permeability and Weissenberg parameter decline to the velocity. An upsurge variable of the thermal conductivity grows to the temperature profile. Compared to the nanofluids, the

hybrid nanofluids have higher thermal efficiency, making them a more effective working fluid. The magnetic field strength significantly reduces the movement and has a striking effect on the width of the momentum boundary layer.

**Keywords:** tangent hyperbolic fluid, cross-diffusion, radiation, magnetohydrodynamic, stretching surface

## Nomenclature

$x, y$	consistent coordinates for $x$ -axis and $y$ -axis
$c > 0$	positive constant
$T(K)$	fluid temperature
$C$	concentration
$\Gamma$	time constant
$n$	power law index
$\rho$	density
$\mu$	dynamic viscosity
$C_p$	specific heat capacity
$C_s$	volume fraction susceptibility
$T_m$	mean fluid parameter
$K_T$	thermal diffusion ratio
$T_w$	temperatures of the surface
$T_\infty$	ambient temperature
$C_w$	concentration of the surface
$C_\infty$	ambient concentration
$D_B$	mass diffusivity
$Q_0$	heat source ( $>0$ )/sink ( $<0$ ) amount
$k_p$	material porousness
hnf	hybrid nanofluid
nf	nanofluid
$f$	base fluid
$C_p$	heat capacity at unvarying pressure
$B_0(\text{Tesla-T})$	magnetic field strength
$M$	shape factor
$\phi_{\text{Cu}}$	volume fraction of Cu

\* **Corresponding author: Karuppusamy Loganathan**, Department of Mathematics and Statistics, Manipal University Jaipur, Jaipur, 303007, Rajasthan, India, e-mail: loganathankaruppusamy304@gmail.com

**Karupiah Senthilvadivu**: Department of Mathematics, K.S. Rangasamy College of Technology, Tiruchengode, 637215, Tamilnadu, India, e-mail: senthilvadivu@ksrct.ac.in

**Mohamed Abbas**: Electrical Engineering Department, College of Engineering, King Khalid University, Abha, 61421, Saudi Arabia, e-mail: mabas@kku.edu.sa

**Mohammed S. Alqahtani**: Radiological Sciences Department, College of Applied Medical Sciences, King Khalid University, Abha, 61421, Saudi Arabia; BioImaging Unit, Space Research Centre, Michael Atiyah Building, University of Leicester, Leicester, LE1 7RH, United Kingdom, e-mail: mosalqhtani@kku.edu.sa

$\phi_{\text{Al}_2\text{O}_3}$	volume fraction of $\text{Al}_2\text{O}_3$
$\sigma^*$	Stefan-Boltzmann constant
$k^*$	coefficient of mean absorption
$f$	nondimensional velocity
$\theta$	nondimensional temperature
$\phi$	nondimensional concentration
$K$	porous medium
$Mn$	Hartmann number
$W$	Weissenberg number
$Ec$	Eckert number
$Q$	heat source parameter
$Pr$	Prandtl number
$Nr$	radiation parameter
$Du$	Dufour number
$Sc$	Schmidt number
$Sr$	Soret number
$C_f$	shear stress
$Nu_x$	local Nusselt number
$Sh_x$	local Sherwood number
$Re_x$	local Reynolds number
$q_r$	radiative heat flux
$S$	extra shear stress
$P$	pressure
$I$	identity vector
$\mu_0$	zero shear rate viscosity
$\mu_\infty$	infinite shear rate viscosity

## 1 Introduction

Non-Newtonian fluids are common in engineering and manufacturing and have undergone a rigorous inspection. These fluids often have complex constituent interactions. Both the stress–strain connection in rheology and the energy–current relationship in thermodynamics are nonlinear for such fluids. One of the non-Newtonian fluids that may adequately describe the shear thinning phenomena is the tangent hyperbolic fluid. Samples of tangent hyperbolic fluids include magma, sauce, cream cheese, blood, and paint. Compared to the alternative formulation for non-Newtonian fluids, this rheological model offers a few benefits such as flexibility, computational ease, and physical resilience. Moreover, rather than being based on an actual relationship, it is derived from the physical laws of liquids. Laboratory studies have shown that this model makes highly accurate predictions about the shear thinning phenomena. Further, this model provides a relatively realistic description of blood flow. A porous material significantly influences how thick the momentum boundary layer is. Hence, numerous investigators have

considered porous media while simulating heat transfer processes in moving fluids.

Nanoliquids have higher heat transfer rates and have several industrial and technical uses, making them of great interest to scientists. As deliberated elsewhere, a popular sort of weird fluid called a hybrid nanofluid suspends deuce or adds different types of metal particles in the regular fluid. Numerous nanoparticles may be deferment in a merged or combination of regular fluids to create hybrid nanofluid. The hybrid nanofluid applies to many heat exchange areas, including transportation, engineering, and health sciences, as deliberated elsewhere. Alumina ( $\text{Al}_2\text{O}_3$ ) is a ceramic substance with several exceptional qualities, including high stability and chemical inertness.  $\text{Al}_2\text{O}_3$ , however, has poorer heat conductivity than metallic nanoparticles. Copper (Cu) and aluminum (Al) metallic nanoparticles have very high thermal conductivities. However, two significant factors – stability and reactivity – always prevent the use of metallic nanoparticles in nanofluid applications. Hybrid nanofluid flow with an oblique magnetic field across a rotating cylinder was investigated by Abbas *et al.* [1]. Heat and mass transport of GO/kerosene oil and GO + Ag/kerosene oil hybrid nanofluids passed through a porous extending sheet were studied by Ahmad *et al.* [2]. Riaz *et al.* [3] investigated the hybridization of the Eyring–Powell nanofluid model with a peristaltic flow. The study was conducted under the assumptions of long wavelength and lubrication approximations. Aladdin *et al.* [4] inspected the magnetohydrodynamics (MHD) hybrid nanofluid flow with suction impact over a permeable moving surface. Ali *et al.* [5] studied the stagnation point flow of tangent hyperbolic hybrid nanofluid over expending sheet. Atif *et al.* [6] examined the variable thermal conductance and radiative impressions on the hydromagnetic tangent hyperbolic fluid hybrid nanoparticles over an extending sheet along with slip and convective circumstances. Awais *et al.* [7] found the entropy generation of unvarying MHD hyperbolic tangent nanofluid flow over a stretchy surface with nonlinear Boussinesq estimate along with the impressions of the viscous dissipation and Joule heating. Dual separate fluids, specifically hybrid nanofluid Cu– $\text{Al}_2\text{O}_3$ /water and nanofluid Cu/water, are castoff to examine the movement and heat transport features over a holey extending sheet in the company of a magnetic field studied by Devi and Devi [8]. Gul *et al.* [9] explored the Cu– $\text{Al}_2\text{O}_3$ /water hybrid nanoparticles over a spreading sheet with the outcome of the magnetic dipole to supervisory the motion and thermal boundary layers. Devi and Devi [10] explored the study on hybrid nanofluid/water, and Cu/water flow passes through an extending sheet.

The Dufour number (diffusion-thermo impact) is regarded as a heat transfer due to the concentration gradient, whereas the Soret effect (thermal-diffusion) is regarded as mass

transport caused by the temperature gradient. These effects hold significant importance in a wide range of fields such as geothermal energy, nuclear waste repositories, and drying technology. Cross-diffusion effects were investigated by Hafeez *et al.* [11] and Kasali *et al.* [12] using non-Newtonian fluids in a variety of geometries. Research conducted by Noreen *et al.* [13] looked into the characteristics of mass transfer that occur during the electroosmotic flow of Jeffrey fluid inside of a microchannel. They came to the conclusion that the Soret number is responsible for reducing the concentration. The mixed convective Carreau fluid flow that occurred across an active vertical plate with cross-diffusion effects was modeled by Gautam *et al.* [14], who offered a framework for the flow. In addition, they observed that the friction factor dropped as the Dufour number climbed. Salleh *et al.* [15] described the phenomena of forced convective nanofluid flow across a very thin needle. This phenomenon was discussed within the context of Dufour and Soret effects.

When there are potential large temperature variations between the surface (such as the spacecraft body) and the fluid around it, the heat source/sink impacts in thermal convection become important. The production of heat is significant when it comes to endothermic or exothermic chemical processes. Hanif *et al.* [16] studied the 2D viscous fluid flow over a flat surface with viscous dissipation impact. Hanif *et al.* [17] inspected the unsteady upper-convected Maxwell hybrid nanofluid flow with a time-fractional derivative and Cattaneo–Christov heat flux. Izady *et al.* [18] studied the 2D MHD radiative  $\text{Fe}_2\text{O}_3$ – $\text{CuO}$ /water hybrid nanofluid flow over a porous stretchy/reduction wedge. Jamshed *et al.* [19] analyzed the thermal transference of  $\text{Cu}$ – $\text{ZrO}_2$ /EG (ethylene glycol) hybrid nanofluid past within solar arms parabolic trough solar gatherer along with numerous impacts such as porous mode, Cattaneo–Christov heat flux, and viscous dissipation. An investigation of the thermal features of radiative  $\text{Cu}$ – $\text{TiO}_2$ /EG over a slippery extended surface along with Joule heating and including changing thermal conductance was examined by Jamshed *et al.* [20]. Khan [21] studied the linear viscoelastic fluid flow over stretching/shrinking sheet with MHD impact. Khan [22] discussed the MHD viscous fluid flow over an extending sheet to outline the coupling of He's polynomials and Laplace transformation. Khan and Mohyud-Din [23] analyzed the effects of variable viscosity and thermal conductivity on the flow and heat transfer in a laminar liquid thin film on a horizontal shrinking/stretching sheet.

Viscous mechanical dissipation effects, which are often indicated by the Eckert number, are significant in geophysical flows as well as in some industrial processes. The biological fluid that is present in living things and is affected by magnetic fields is known as the bio-magnetic

fluid. One of the most prevalent types of bio-magnetic fluids is blood. Due to its significant uses in bioengineering and the medical sciences such as the development of magnetic devices for cell separation, the reduction of surgical bleeding, and the targeted delivery of medications, researchers have focused more on bio magnetic fluid studies in recent decades. In addition, certain components of the human body can be imaged using magnetic particles during magnetic resonance imaging or during cancer therapy.

The MHD Darcy–Forchheimer flow of a third-grade nanofluid over a linearly stretchable sheet was investigated by Khan *et al.* [24]. Loganathan *et al.* [25] explored the entropy investigation of radiative third-order nanofluid slipping flow over a stretchy sheet fixed in a porous plate along with non-Fourier heat flux and nanoparticle volume fraction in zero mass flux situations. Madhukesh *et al.* [26] investigated a curved stretchy sheet with non-Fourier heat flux model, Newtonian heating, and continuous wall temperature over a water-based AA7072–AA7075 hybrid nanofluid. Nadeem *et al.* [27] studied the heat transfer rate of unsteady tangent hyperbolic fuzzy hybrid nanofluid flow over an exponentially extending surface. An investigation of the heat and mass transference in 3D hydromagnetic radiative  $\text{Al}_2\text{O}_3$ – $\text{Ag}$ /water-based hybrid nanofluid flow through a stretchy sheet was investigated by Shoab *et al.* [28]. Suresh *et al.* [29] analyzed the heat transference rate of a  $\text{Cu}$ – $\text{Al}_2\text{O}_3$ /blood-based hybrid nanofluid flow. Ullah *et al.* [30] inspected the hydromagnetic tangent hyperbolic fluid flow along an extending sheet in the suction/blowing upshot attendance. Venkateswarlu and Satya Narayana [31] worked on the momentum impressions of inconstant viscidness and viscous dissipation on a permeable extending sheet in the company of radiative  $\text{Cu}$ – $\text{Al}_2\text{O}_3$ /H<sub>2</sub>O hybrid nanofluid.

Based on the previous research, this research aims to fill a gap by investigating the flow, thermal, and mass features of an MHD radiative tangent hyperbolic hybrid nanofluid structure that passes over a porous stretching surface with some objectives:

- What are the impacts of viscous dissipation, and heat source/sink on hybrid and nanofluid flow?
- What is the impact of the cross-diffusion?
- How the flow, heat, and mass transfer affect by  $\text{Al}_2\text{O}_3$  and  $\text{Cu}$  nanoparticles with blood base fluid?

The suitable symmetry variables are utilized to transform the standard tangent hyperbolic fluid equations into potential ordinary differential equations (ODEs). The ODEs will then be mathematically explained using the BVP4C method for the parametrical effects. The study results were presented in graphical and tabular forms for technical debates. We carefully considered the impacts of cross-

diffusion, hydromagnetic parameters, viscous-based dissipation, joule heating, and morphologies of the suspended particles under thermal radiation exposed to boundary conditions.

## 2 Mathematical formulation

### 2.1 Concept of tangential hyperbolic constitutive

Only one mathematical model cannot account for all the rheological working fluids. The works cover a range of fluid models that address various fluid characteristics. The four-constant tangent hyperbolic fluid model can accurately designate the effects of shear thinning. Between zero shear rate and infinite shear rate, the apparent viscosity changes. The fundamental formula for the tangent hyperbolic fluid is provided by the following equations [6,20]:

$$S = -PI + \tau, \quad (1)$$

$$\tau = [\mu_\infty + (\mu_0 + \mu_\infty) \tanh(\Gamma\dot{\Omega})^n] \dot{\Omega}. \quad (2)$$

The shear rate  $\dot{\Omega}$  [3,6] is assumed by

$$\dot{\Omega} = \sqrt{\frac{1}{2} \sum_i \sum_j \dot{\Omega}_{ij} \dot{\Omega}_{ij}} = \sqrt{\frac{1}{2} \Pi}, \quad (3)$$

where  $\Pi$  is the second invariant strain rate [3,6] tensor and is specified by

$$\Pi = \frac{1}{2} \text{tr}[\text{grad}V + (\text{grad}V)^T]^2. \quad (4)$$

Given that we are concentrating on the shear thinning fluid behavior and that we assume  $\mu_\infty = 0$ , the additional stress tensor  $\tau$  for  $\Gamma\dot{\Omega} < 1$  simplifies to,

$$\begin{aligned} \tau &= \mu_0 [(\Gamma\dot{\Omega})^n] \dot{\Omega} = \mu_0 [(1 + \gamma\dot{\Omega} - 1)^n] \dot{\Omega} \\ &= \mu_0 [1 + n(\gamma\dot{\Omega} - 1)] \dot{\Omega}. \end{aligned} \quad (5)$$

The flow model is based on the preceding conditions and objectives:

- 2D time-independent nonlinear incompressible laminar boundary layer flow.
- A porous stretching sheet is measured about to the  $x$ -axis and erects to the  $y$ -axis.
- A constant magnetic field and joule heating is measured.
- Radiative tangent hyperbolic hybrid nanofluid.
- Flow with heat source and viscous dissipation.
- Cross-diffusion impacts are addressed.

The geometrical fluid flow setup is shown in Figure 1.

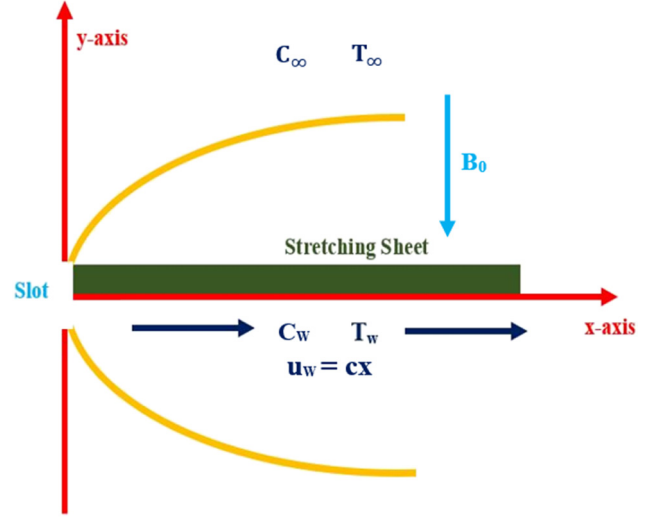


Figure 1: Movement model picture.

The following equations are the ones that have been found to control previous studies [6,9,28]:

$$\frac{\partial u}{\partial x} + \frac{\partial v}{\partial y} = 0, \quad (6)$$

$$\begin{aligned} \rho_{\text{hnf}} \left( u \frac{\partial u}{\partial x} + v \frac{\partial u}{\partial y} \right) &= \mu_{\text{hnf}} \left[ (1-n) + n\sqrt{2}\Gamma \frac{\partial u}{\partial y} \right] \frac{\partial^2 u}{\partial y^2} \\ &\quad - \sigma_{\text{hnf}} B_0^2 u - \mu_{\text{hnf}} \frac{u}{k_p}, \end{aligned} \quad (7)$$

$$\begin{aligned} (\rho C_p)_{\text{hnf}} \left( u \frac{\partial T}{\partial x} + v \frac{\partial T}{\partial y} \right) &= \frac{\partial}{\partial y} \left[ k_{\text{hnf}}^* \frac{\partial T}{\partial y} \right] + \mu_{\text{hnf}} \frac{n\Gamma}{\sqrt{2}} \frac{\partial u}{\partial y} \left( \frac{\partial u}{\partial y} \right)^2 \\ &\quad + \mu_{\text{hnf}} (1-n) \left( \frac{\partial u}{\partial y} \right)^2 - \frac{\partial q_r}{\partial y} + Q_0 (T - T_\infty) + \sigma_{\text{hnf}} B_0^2 u^2 \\ &\quad + \frac{D_B K_T}{C_s C_p} \frac{\partial^2 C}{\partial y^2}, \end{aligned} \quad (8)$$

$$u \frac{\partial C}{\partial x} + v \frac{\partial C}{\partial y} = (D_B)_{\text{hnf}} \frac{\partial^2 C}{\partial y^2} + \frac{D_B K_T}{T_m} \frac{\partial^2 T}{\partial y^2}. \quad (9)$$

The present examples have the following boundary circumstances [10]:

$$u = u_w = cx; v = 0; T = T_w; C = C_w; \text{ at } y = 0.$$

$$u \rightarrow 0; T \rightarrow T_\infty; C \rightarrow C_\infty; \text{ at } y \rightarrow \infty. \quad (10)$$

Each variable in the process is named and described in the Nomenclature section, and the topographic formulas for nanoparticles are shown in Table 1.

**Table 1:** Nanofluid and hybrid nanofluid formulation constraints in the system, as mentioned earlier in the equations [23]

Thermal properties	Nanofluid	Hybrid nanofluid
Thermal diffusivity	$\alpha_{\text{nf}} = \frac{k_{\text{nf}}}{(\rho C_p)_{\text{nf}}}$	$\alpha_{\text{hnf}} = \frac{k_{\text{hnf}}}{(\rho C_p)_{\text{hnf}}}$
Viscosity	$\frac{\mu_{\text{nf}}}{\mu_f} = \frac{1}{(1 - \phi_{\text{Al}_2\text{O}_3})^{2.5}}$	$\frac{\mu_{\text{hnf}}}{\mu_f} = \frac{1}{(1 - \phi_{\text{Cu}})^{2.5}(1 - \phi_{\text{Al}_2\text{O}_3})^{2.5}}$
Heat capacity	$\frac{(\rho C_p)_{\text{nf}}}{(\rho C_p)_f} = \left( (1 - \phi_{\text{Al}_2\text{O}_3}) + \phi_{\text{Al}_2\text{O}_3} \frac{(\rho C_p)_{\text{Al}_2\text{O}_3}}{(\rho C_p)_f} \right)$	$\frac{(\rho C_p)_{\text{hnf}}}{(\rho C_p)_f} = \phi_{\text{Cu}} \frac{(\rho C_p)_{\text{Cu}}}{(\rho C_p)_f} + (1 - \phi_{\text{Cu}}) \left( (1 - \phi_{\text{Al}_2\text{O}_3}) + \phi_{\text{Al}_2\text{O}_3} \frac{(\rho C_p)_{\text{Al}_2\text{O}_3}}{(\rho C_p)_f} \right)$
Density	$\frac{(\rho)_{\text{nf}}}{(\rho)_f} = \left( (1 - \phi_{\text{Al}_2\text{O}_3}) + \phi_{\text{Al}_2\text{O}_3} \frac{(\rho)_{\text{Al}_2\text{O}_3}}{(\rho)_f} \right)$	$\frac{(\rho)_{\text{hnf}}}{(\rho)_f} = \phi_{\text{Cu}} \frac{(\rho)_{\text{Cu}}}{(\rho)_f} + (1 - \phi_{\text{Cu}}) \left( (1 - \phi_{\text{Al}_2\text{O}_3}) + \phi_{\text{Al}_2\text{O}_3} \frac{(\rho)_{\text{Al}_2\text{O}_3}}{(\rho)_f} \right)$
Thermal conductivity	$k_{\text{nf}} = \frac{k_{\text{Al}_2\text{O}_3} + (M - 1)k_f - (M - 1)\phi_{\text{Al}_2\text{O}_3}(k_f - k_{\text{Al}_2\text{O}_3})}{k_{\text{Al}_2\text{O}_3} + (M - 1)k_f + \phi_{\text{Al}_2\text{O}_3}(k_f - k_{\text{Al}_2\text{O}_3})} k_f$	$k_{\text{hnf}} = \frac{k_{\text{Cu}} + (M - 1)k_{\text{nf}} - (M - 1)\phi_{\text{Cu}}(k_{\text{nf}} - k_{\text{Cu}})}{k_{\text{Cu}} + (M - 1)k_{\text{nf}} + \phi_{\text{Cu}}(k_{\text{nf}} - k_{\text{Cu}})} k_{\text{nf}}$
Electrical conductivity	$\sigma_{\text{nf}} = \left( 1 + \frac{3 \left( \frac{\phi_{\text{Al}_2\text{O}_3} \sigma_{\text{Al}_2\text{O}_3}}{\sigma_f} - (\phi_{\text{Al}_2\text{O}_3}) \right)}{\left( \frac{\phi_{\text{Al}_2\text{O}_3} \sigma_{\text{Al}_2\text{O}_3}}{(\phi_{\text{Al}_2\text{O}_3} \sigma_f + 2)} - \left( \frac{\phi_{\text{Al}_2\text{O}_3} \sigma_{\text{Al}_2\text{O}_3}}{\sigma_f} - (\phi_{\text{Al}_2\text{O}_3}) \right) \right)} \right)$	$\sigma_{\text{hnf}} = \frac{\sigma_{\text{Cu}} + (M - 1)\sigma_{\text{nf}} - (M - 1)\phi_{\text{Cu}}(\sigma_{\text{nf}} - \sigma_{\text{Cu}})}{\sigma_{\text{Cu}} + (M - 1)\sigma_{\text{nf}} + \phi_{\text{Cu}}(\sigma_{\text{nf}} - \sigma_{\text{Cu}})} \sigma_{\text{nf}}$

Table 1 lists the pure working fluid and two nanomaterials' formulations (Table 2).

Table 3 also highlights the various shape factor coefficients and different shapes of nanoparticles.

The thermal conductivity of nanoparticles combination is reputed as [6,9]

$$k^*_{\text{hnf}} = k_{\text{hnf}} \left[ 1 + \xi \frac{T - T_\infty}{T_w - T_\infty} \right]. \tag{11}$$

The Al<sub>2</sub>O<sub>3</sub> blends the hybrid nanofluid and Cu suspended in the blood. The adequate small volume  $\phi_{\text{Cu}}$  and  $\phi_{\text{Al}_2\text{O}_3}$  are made secure at 0.03 and 0.01, respectively, throughout the study.

The penultimate term in energy Eq. (8), the radiative heat flux, denoted by  $q_r$ , is outlined by the Rosseland approximation [6,9]:

$$q_r = \frac{-4\sigma^*}{3k^*} \frac{\partial T^4}{\partial y}. \tag{12}$$

Next, we can approximate the form by using the Taylor series for the term  $T^4$  at a location  $T_\infty$  and ignoring the higher order terms.

By using Taylor's arrangement extension about  $T_\infty$  and ignoring advancing terms, we can express  $T^4$  as a linear connection of temperature; thus,

**Table 2:** Cu–Al<sub>2</sub>O<sub>3</sub>/blood hybrid nanoparticles' physical properties [10]

Physical characteristics	Blood	Cu	Al <sub>2</sub> O <sub>3</sub>
$\rho$	1,060	8,933	3,970
$C_p$	3,770	385.0	765
$k$	0.492	401.00	40
$\sigma$	$4.3 \times 10^{-5}$	$5.96 \times 10^7$	$35 \times 10^6$
Pr	24	—	—

$$T^4 \approx 4T_\infty^3 T - 3T_\infty^4. \tag{13}$$

Consideration of the following symmetry variables may help us conduct a more efficient model analysis in the present context [12]






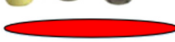
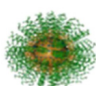
$$\eta = \sqrt{\frac{c}{v_f}} y, \quad v = -\sqrt{c v_f} f, \quad u = c x f', \quad \theta(\eta) = \frac{T - T_\infty}{T_w - T_\infty},$$

and

$$\phi(\eta) = \frac{C - C_\infty}{C_w - C_\infty}. \tag{14}$$

Pseudo-similarity variables can now be differentiated using primes.

**Table 3:** The form factor coefficient ( $M$ ) for various nanoparticle shapes [9]

Types of nanoparticles	Shape	Shape factor
Sphere		3
Hexahedron		3.7221
Tetrahedron		4.0613
Cylinder		4.9
Column		6.3698
Blades		8.6
Lamina		16.1576



Using the similarity modifications Eq. (14), controlling Eqs. (6)–(10) are created where complete satisfaction of the continuity Eq. (6) is attained, and the remaining necessary equations take the following dimensionless form:

$$f'''[(1-n) + nWf''] = \frac{v_f}{v_{\text{hnf}}}(f')^2 + \left(\frac{\sigma_{\text{hnf}}/\sigma_f}{\mu_{\text{hnf}}/\mu_f}\right)Mnf' + Kf' - \frac{v_f}{v_{\text{hnf}}}ff'' = 0, \quad (15)$$

$$\begin{aligned} & \theta'' \left( 1 + \xi\theta + \frac{1}{k_{\text{hnf}}/k_f} \text{PrNr} \right) \\ &= (-1)\text{Pr} \left[ \frac{\rho C_{\text{p hn f}}/\rho C_{\text{p f}}}{k_{\text{hnf}}/k_f} f\theta' + \frac{\mu_{\text{hnf}}/\mu_f}{k_{\text{hnf}}/k_f} \frac{n}{2} W \text{Ec} f'^2 \right. \\ &+ \frac{\mu_{\text{hnf}}/\mu_f}{k_{\text{hnf}}/k_f} \text{Ec}(1-n)f'^2 + \frac{1}{k_{\text{hnf}}/k_f} Q\theta + \xi\theta'^2 \\ &+ \left. \frac{\sigma_{\text{hnf}}/\sigma_f}{k_{\text{hnf}}/k_f} \text{MnEc} f'^2 + \frac{\rho C_{\text{p hn f}}/\rho C_{\text{p f}}}{k_{\text{hnf}}/k_f} \text{Du}\phi'' \right], \quad (16) \end{aligned}$$

$$\phi'' = (-1)\text{Sc}(f\phi' + \text{Sr}\theta'')/(D_{\text{B hn f}}/D_{\text{B f}}) \quad (17)$$

with the boundary circumstances:

$$f(0) = 0, f'(0) = 1, \theta = 1, \phi = 1, \text{ at } \eta = 0.$$

$$f'(\infty) \rightarrow 0, \theta(\infty) \rightarrow 0, \phi(\infty) \rightarrow 0, \text{ at } \eta \rightarrow \infty. \quad (18)$$

Dimensionless constraints in Eqs. (10)–(12) are described using the following notation. These factors are given in the following numerical form:

$$K = \frac{v_f}{ck_p}, \text{ Mn} = \frac{\sigma_f B_0^2}{\rho_f c}, W = \Gamma X \sqrt{\frac{2c^3}{v_f}}, \text{ Ec} = \frac{u_w^2}{(C_p)_f(T_w - T_\infty)},$$

$$Q = \frac{Q_0}{(\rho C_p)_f c}, \text{ Pr} = \frac{v_f}{\alpha_f}, \text{ Nr} = \frac{16\sigma^* T_\infty^3}{3k^* v_f (\rho C_p)_f},$$

$$\text{Du} = \frac{D_m K_T C_w - C_\infty}{c_s c_p v_f T_w - T_\infty}, \text{ Sc} = \frac{v_f}{D_{Bf}}, \text{ and Sr} = \frac{D_m K_T T_w - T_\infty}{T_m v_f C_w - C_\infty}.$$

The shear stress, heat transport rate, and mass transport rate are the physical quantities of practical importance in engineering, and they are defined as follows:

The shear stress is  $C_f = \frac{\tau_w}{\rho_f U_w^2}$ , the Nusselt number is well-defined as  $\text{Nu}_x = \frac{xq_w}{k_f(T_w - T_\infty)}$ , and the Sherwood number  $\text{Sh}_x = \frac{xj_w}{D_{Bf}(C_w - C_\infty)}$ .

The surface shear stress  $\tau_w$  is assumed by  $\tau_w = \mu_{\text{hnf}} \left( \frac{\partial u}{\partial y} \right)_{y=0}$ , and we obtain

$$C_f \text{Re}_x^{1/2} = (\mu_{\text{hnf}}/\mu_f)((1-n)f''(0) + \left(\frac{n}{2}\right)Wf'^2). \quad (19)$$

The rate of heat transfer  $q_w$  is assumed by  $q_w = -k_{\text{hnf}} \left( \frac{\partial T}{\partial y} \right)_{y=0} + (q_r)_{y=0}$ , and we obtain

$$\text{Nu}_x \text{Re}_x^{-1/2} = (-1)(k_{\text{hnf}}/k_f)(1 + \text{Nr})\theta'(0). \quad (20)$$

The rate of mass transfer  $j_w$  is assumed by  $j_w = -D_{\text{B hn f}} \left( \frac{\partial C}{\partial y} \right)_{y=0}$ , and we obtain

$$\text{Sh}_x \text{Re}_x^{-1/2} = (-1)(D_{\text{B hn f}}/D_{\text{B f}})\phi'(0), \quad (21)$$

where  $\text{Re}_x = \frac{xu_w}{v_f}$  is the Reynolds number.

## 2.2 Numerical structure

The equations are solved using the `bvp4c` method. The use of MATLAB software to generate the table and the figures is detailed. Let  $f = y(1)$ ,  $f' = y(2)$ ,  $f'' = y(3)$ ,  $\theta = y(4)$ ,  $\theta' = y(5)$ ,  $\phi = y(6)$ , and  $\phi' = y(7)$ .

Eqs. (15)–(18) reduce into newform as follows:

$$\begin{aligned} & f'''[(1-n) + nWy(3)] \\ &= \frac{v_f}{v_{\text{hnf}}}(y(2))^2 + \left(\frac{\sigma_{\text{hnf}}/\sigma_f}{\mu_{\text{hnf}}/\mu_f}\right)Mny(2) + Ky(2) \\ & - \frac{v_f}{v_{\text{hnf}}}y(1)y(3) = 0, \quad (22) \end{aligned}$$

$$\begin{aligned} & \theta'' \left( 1 + \xi y(4) + \frac{1}{k_{\text{hnf}}/k_f} \text{PrNr} \right) \\ &= (-1)\text{Pr} \left[ \frac{\rho C_{\text{p hn f}}/\rho C_{\text{p f}}}{k_{\text{hnf}}/k_f} y(1)y(5) + \frac{\mu_{\text{hnf}}/\mu_f}{k_{\text{hnf}}/k_f} \frac{n}{2} W \text{Ec} y(3)^3 \right. \\ &+ \frac{\mu_{\text{hnf}}/\mu_f}{k_{\text{hnf}}/k_f} \text{Ec}(1-n)y(3)^2 + \frac{1}{k_{\text{hnf}}/k_f} Qy(4) + \xi y(5)^2 \\ &+ \left. \frac{\sigma_{\text{hnf}}/\sigma_f}{k_{\text{hnf}}/k_f} \text{MnEc} y(2)^2 + \frac{\rho C_{\text{p hn f}}/\rho C_{\text{p f}}}{k_{\text{hnf}}/k_f} \text{Du}\phi'' \right], \quad (23) \end{aligned}$$

$$\phi'' = (-1)\text{Sc}(y(1)y(6) + \text{Sr}\theta'')/(D_{\text{B hn f}}/D_{\text{B f}}), \quad (24)$$

with the boundary circumstances:

**Table 4:** Analyses of Pr and  $\theta'(0)$  values in the absence of other remaining parameters

Pr	Devi and Devi [10] (Runge–Kutta–Fehlberg integration method)	Present study (BVP4C solver)
1	—	0.582010509
2	0.91135	0.911352752
6.13	1.75968	1.759681708
7	1.89540	1.895400400
10	—	2.308001329
20	3.35390	3.353901837

$$y_0(1) = 0, y_0(2) = 1, y_0(4) = 1, y_0(6) = 1, \text{ at } \eta = 0.$$

$$y^\infty(2) \rightarrow 0, y^\infty(4) \rightarrow 0, y^\infty(6) \rightarrow 0 \text{ at } \eta \rightarrow \infty. \quad (25)$$

The choice  $\eta(\infty) = 8$  for a desired accuracy and a converge criterion of  $10^{-5}$  is satisfied for various parameters (from  $10^{-5}$ , the border remained constant).

### 2.3 Code validation

Current findings are verified by comparing them to recent studies. The known research consistency comparison is presented in Table 4. However, the present analysis yields extremely precise results.

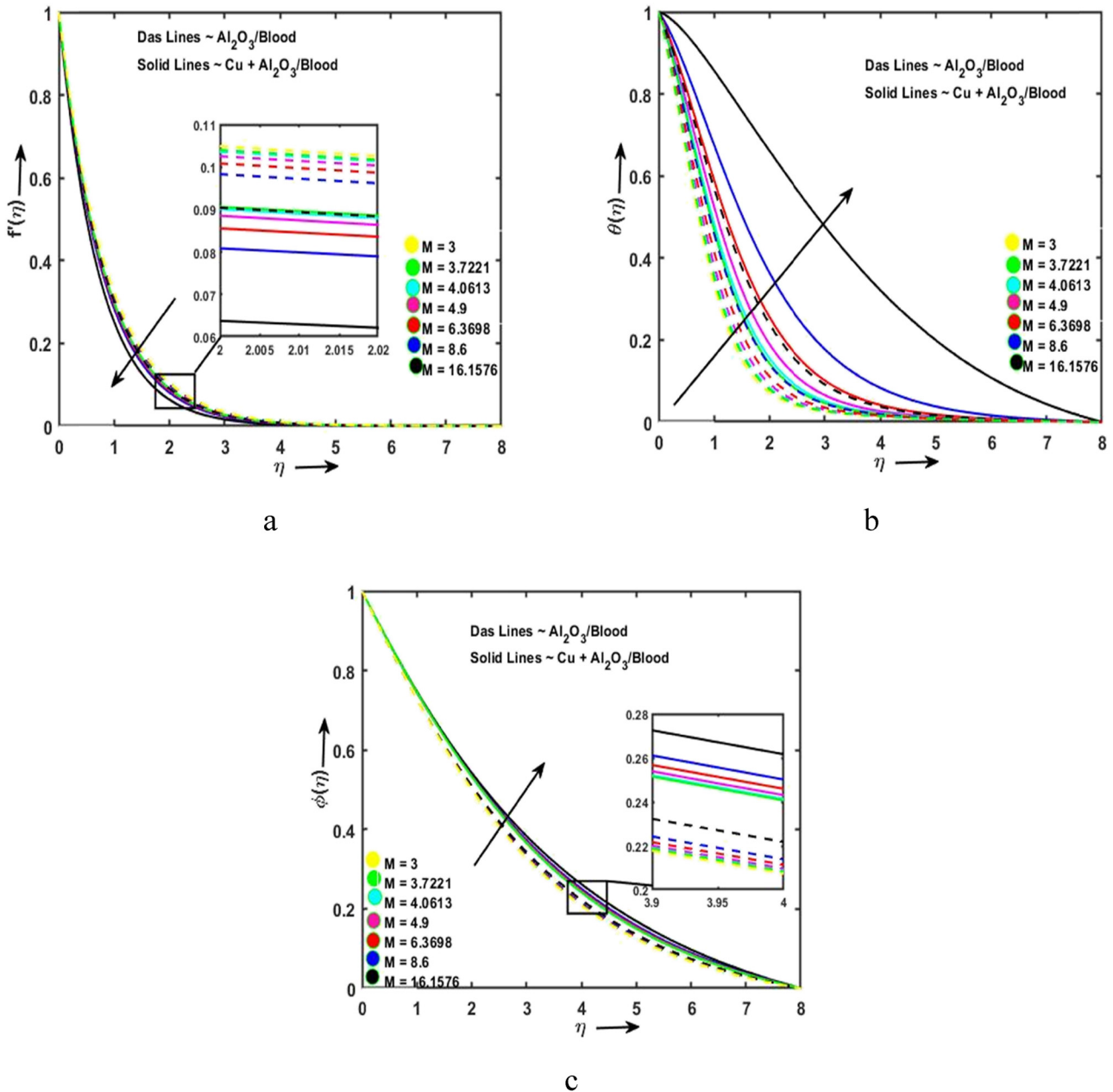
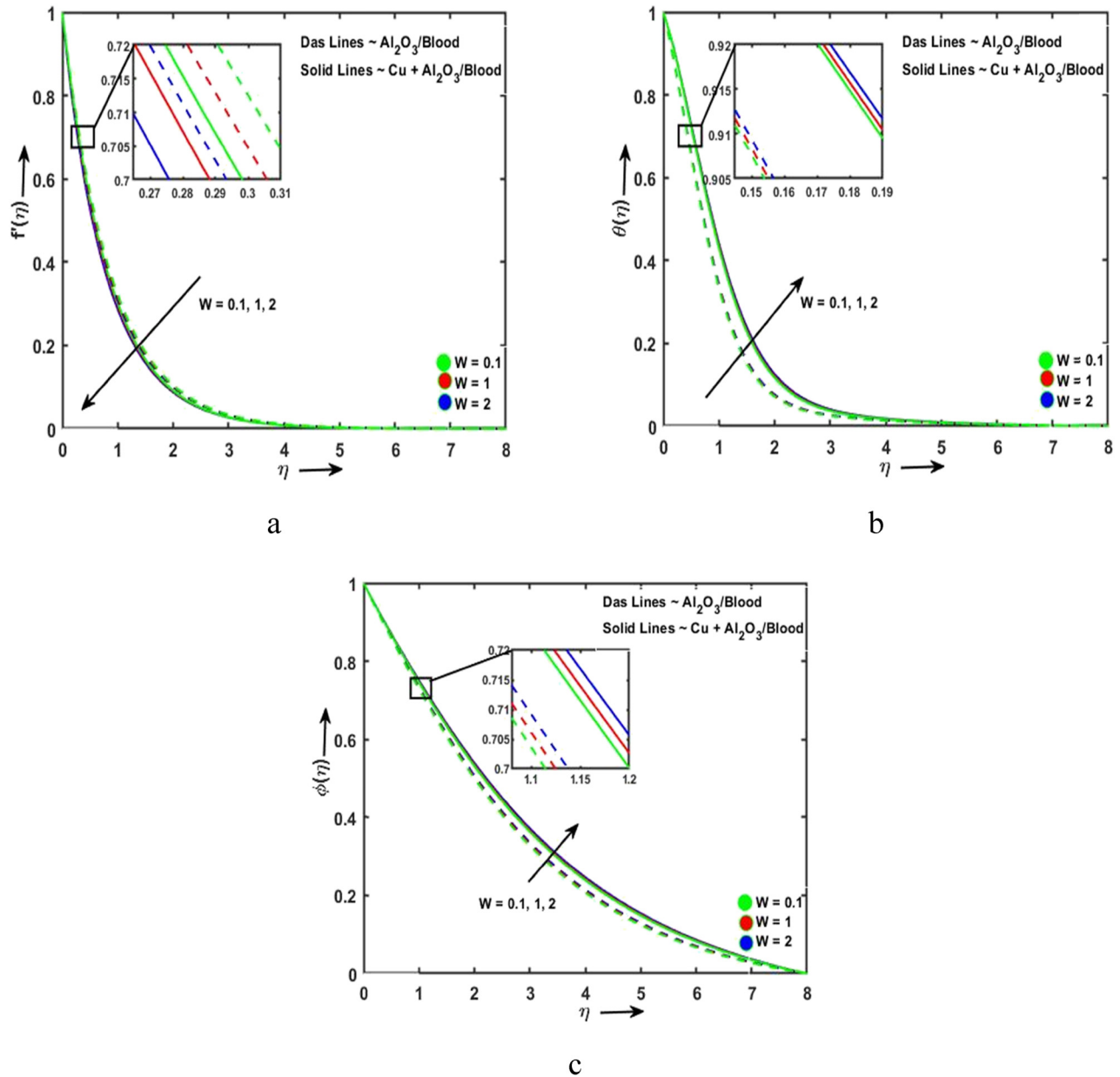


Figure 2: Variance outlines of shape factors. (a)  $f(\eta)$ , (b)  $\theta(\eta)$  and (c)  $\phi(\eta)$ .



**Figure 3:** Variance outlines of  $W$ . (a)  $f(\eta)$ , (b)  $\theta(\eta)$  and (c)  $\phi(\eta)$ .

### 3 Result and discussion

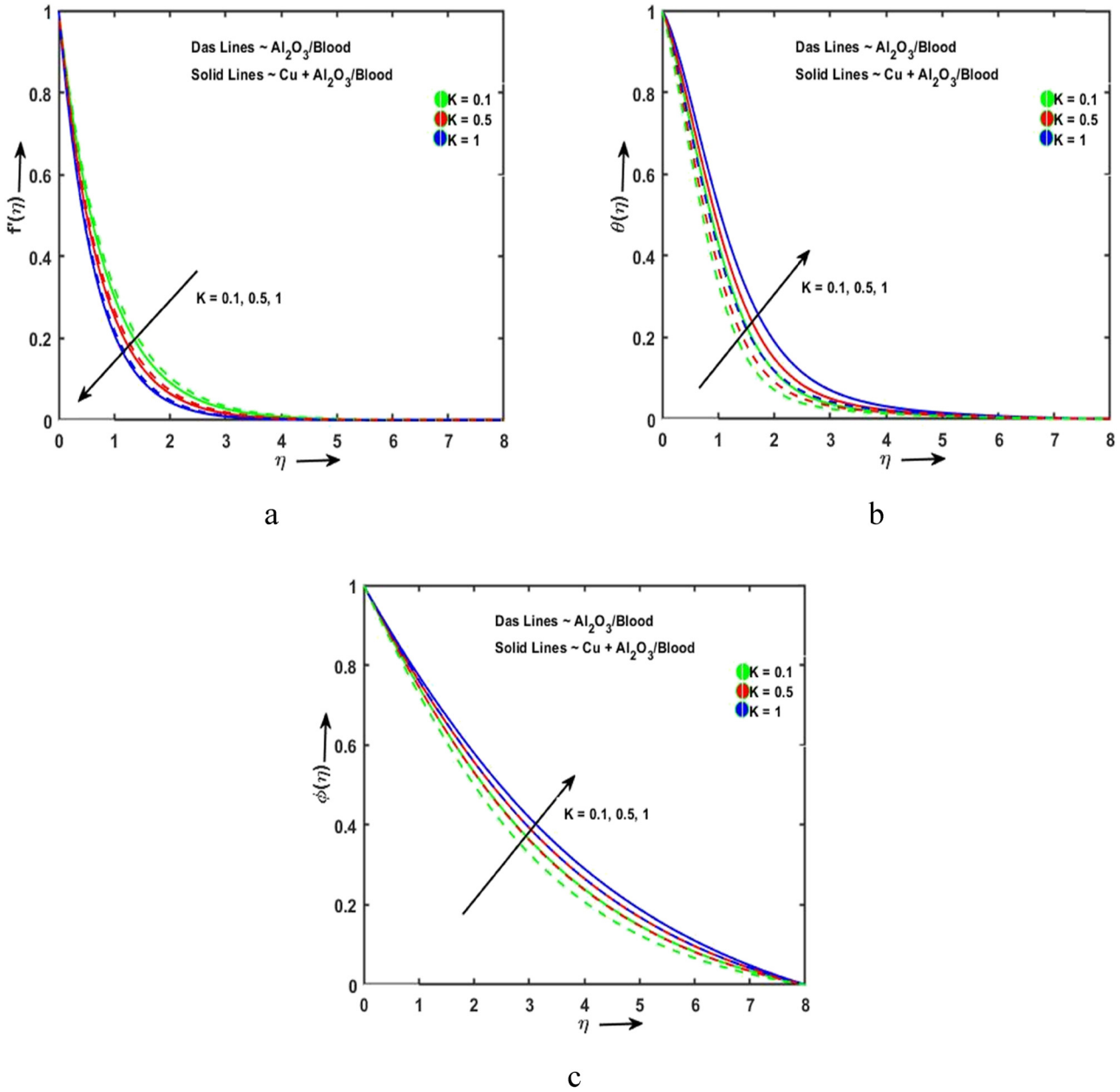
In industrial and biological processes, such as lubricants, emulsions, cancer therapy, biofluids in biological polymer and tissue, drug transportation, nuclear fuel slurries, cancer tumor treatment, and bio-medical fluids, the thermal radiation and magnetic fields with heat transfer containing blood-based nanoparticles become essential. Utilizing the BVP4C methodology, the attributes of two blood-based nanofluids,

$\text{Al}_2\text{O}_3/\text{blood}$  and  $\text{Al}_2\text{O}_3\text{-Cu}/\text{blood}$  are quantitatively investigated. The implications of developing flow features have been listed utilizing a variety of data obtained through

graphs and tables. The domain of nanoparticles is 0.01–0.03% used in this current fluid flow. Using MATLAB, we explore how changes in variables including speed, temperature, concentration, skin-friction quantity, Nusselt parameter, and Sherwood number might affect the final results are shown in Figures 2–13 and Tables 5 and 6. The values of the physical parameters were determined as follows for the current study:  $M = 3$ ,  $Mn = Sc = 0.5$ ,  $K = W = \xi = Ec = Q = Nr = Du = Sr = n = 0.1$ ,  $\phi_{\text{Al}_2\text{O}_3} = 0.01$ ,  $\phi_{\text{Cu}} = 0.03$ , and  $Pr = 24$ .

Figure 2 illustrates the impressions of nanomaterial shape factors on motion, temperature, and concentration for both nf and hnf. Figure 2a depicts the decline motion



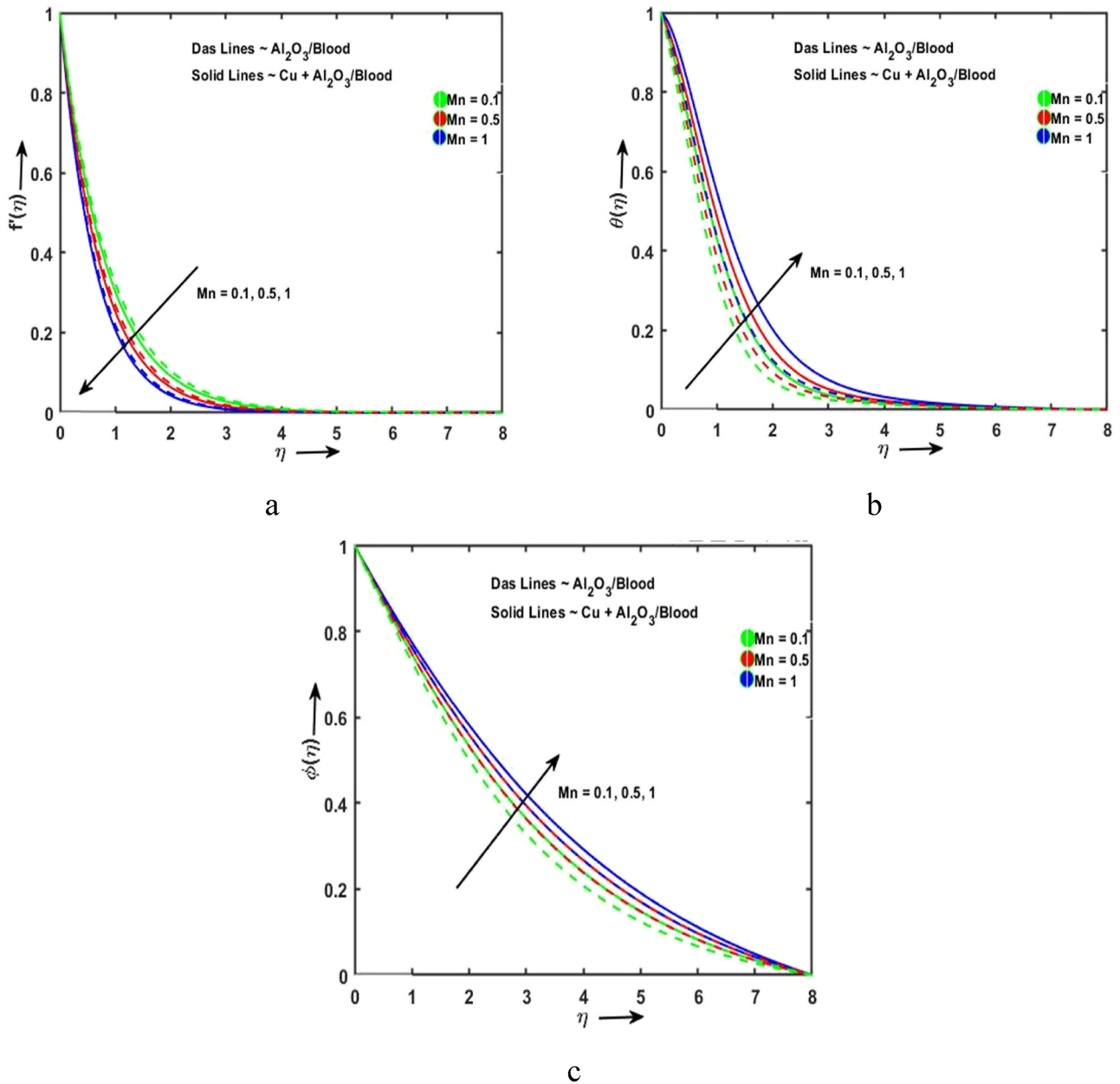


**Figure 4:** Variance outlines of  $K$ . (a)  $f(\eta)$ , (b)  $\theta(\eta)$  and (c)  $\phi(\eta)$ .

impact; Figure 2b and c shows the upsurge thermal and volume fraction impressions for various nanoparticle shapes, respectively. The shape variety was created, starting with spherical, moving through hexahedron, tetrahedron, cylinder, column, blades, and lamina. Physically, these modifications were made in the following sequence depending on how well they transmitted heat. Figure 3a shows the declining motion impressions of increasing Weissenberg parameter for both nf and hnf. The increased Weissenberg number causes the flowing fluid to be more challenging to move by increasing its viscosity and friction. Weissenberg number, in terms of

physics, is the proportion of relaxation time to processing time. An increasing value of  $W$  signifies a rise in relaxation time, which reduces the fluid movement. An increasing impression of temperature and concentration of Weissenberg parameter is shown in Figure 3b and c, respectively. A temperature increases due to the direct relationship between the Williamson parameter and time.

Figure 4a–c depict the motion, temperature, and concentration variances with the upsurge permeability parameter for nf and hnf, respectively. The movement decreases with upsurge permeability, while opposite impressions are seen for



**Figure 5:** Variance outlines of Mn. (a)  $f(\eta)$ , (b)  $\theta(\eta)$  and (c)  $\phi(\eta)$ .

temperature and concentration. Porous media increases the fluid flow restriction, which slows the flow down. Figure 4b illustrates the temperature increases with the increasing permeability parameter due to the thickening thermal boundary layer. This is clear from the opposition of the porous medium to fluid motion. The flow is provided with resistance, which raises the temperature.

The magnetic parameter declines motion, upsurges temperature, and upsurges volume fraction impacts, which are shown in Figure 5a–c, respectively. The width of the motion and momentum boundary layer depreciates as the magnetic impact upsurges due to the opposite Lorentz force, as shown

in Figure 5a. The well-known thermal dispersion for the  $Al_2O_3-Cu/blood$  hybrid class fluid and the  $Al_2O_3/blood$  nano class fluid is shown in Figure 5b. The hybrid class fluid has another factor contributing to its more significant performance in thermal transference in addition to its improved thermal transmitting abilities. The slower the flow, the more time it has to go over the surface and collect more heat. This is also a factor in the  $Al_2O_3-Cu/blood$  hybrid fluid’s enhanced heat transfer rate. The impact of magnetic parameters on the concentration profiles is shown in Figure 5c. As can be observed, the magnitude of concentration profiles rises as

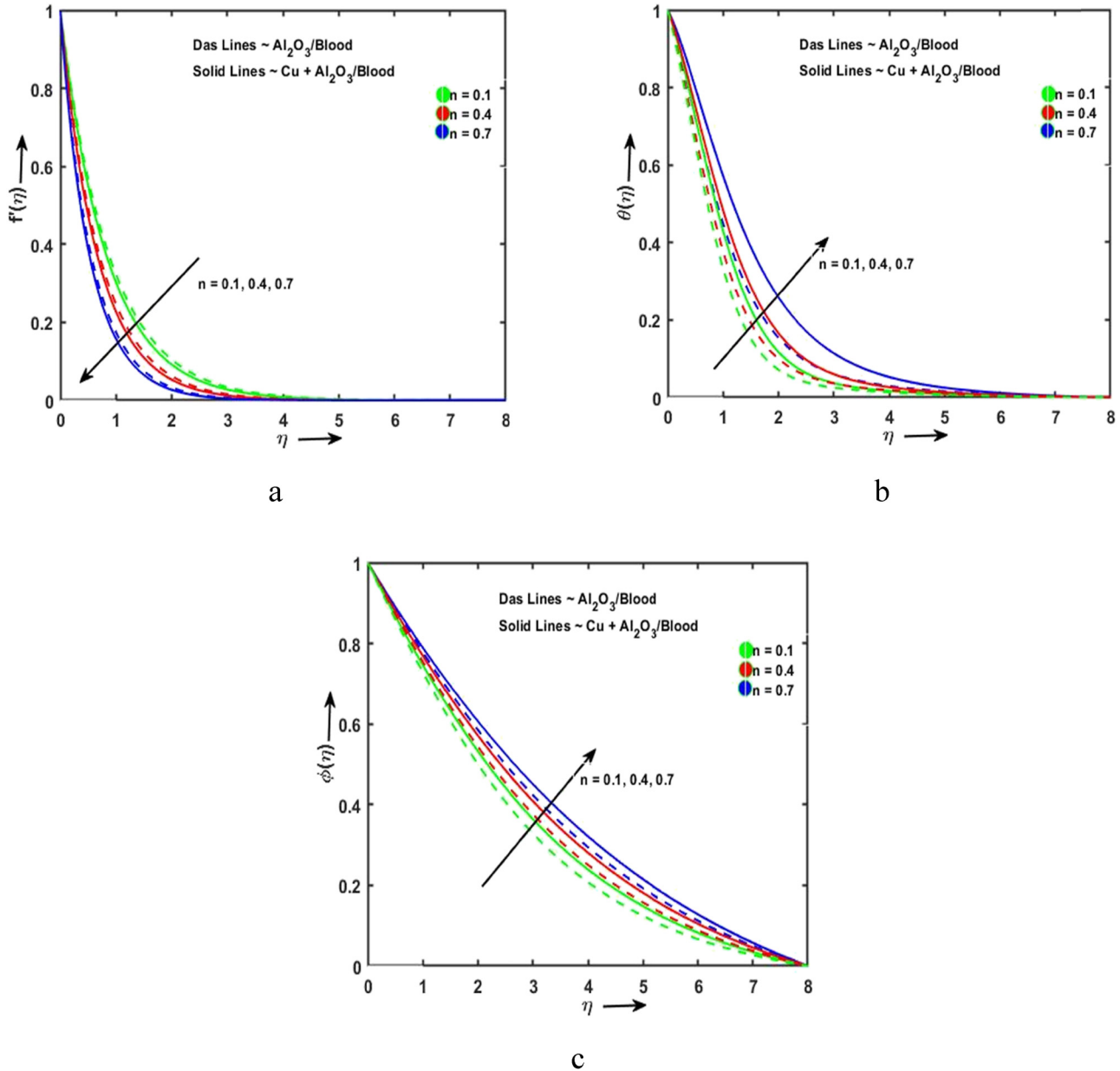


Figure 6: Variation outlines of  $n$ . (a)  $f(\eta)$ , (b)  $\theta(\eta)$  and (c)  $\phi(\eta)$ .

the magnetic parameter increases. As previously established, a rise in the magnetic parameter causes the speed of the boundary layer to be smaller. As a result, the reduced speed of the boundary layer encourages the diffusion of nanoparticles there.

Figure 6a shows the falloff motion impacts of the power law index for both nf and hnf. When the power law index  $n$  rises, it means that the viscosity of the fluid is growing. As a result, the fluid speed decreases, but the concentration and temperature sectors increase. Figure 6b and c demonstrates how growing the quantity of the power-law index parameter raises the temperature

and concentration. This happens because the nature of the fluid switches from shear thickening to shear thinning at higher values of  $m$ .

An upsurge impression of motion, temperature, and concentration for volume fractions of Al<sub>2</sub>O<sub>3</sub> and Cu is shown in Figure 7a–c, respectively. As the volume percentage of nanoparticles rises, the momentum boundary layers thicken, and the velocity increases (Figure 7a). This is consistent with the physical behavior; as the volume of Cu and Al<sub>2</sub>O<sub>3</sub> nanoparticles grows, thermal conductivity rises as well, resulted in a thickening of the thermal boundary layer, and therefore, the temperature increases (Figure 7b).

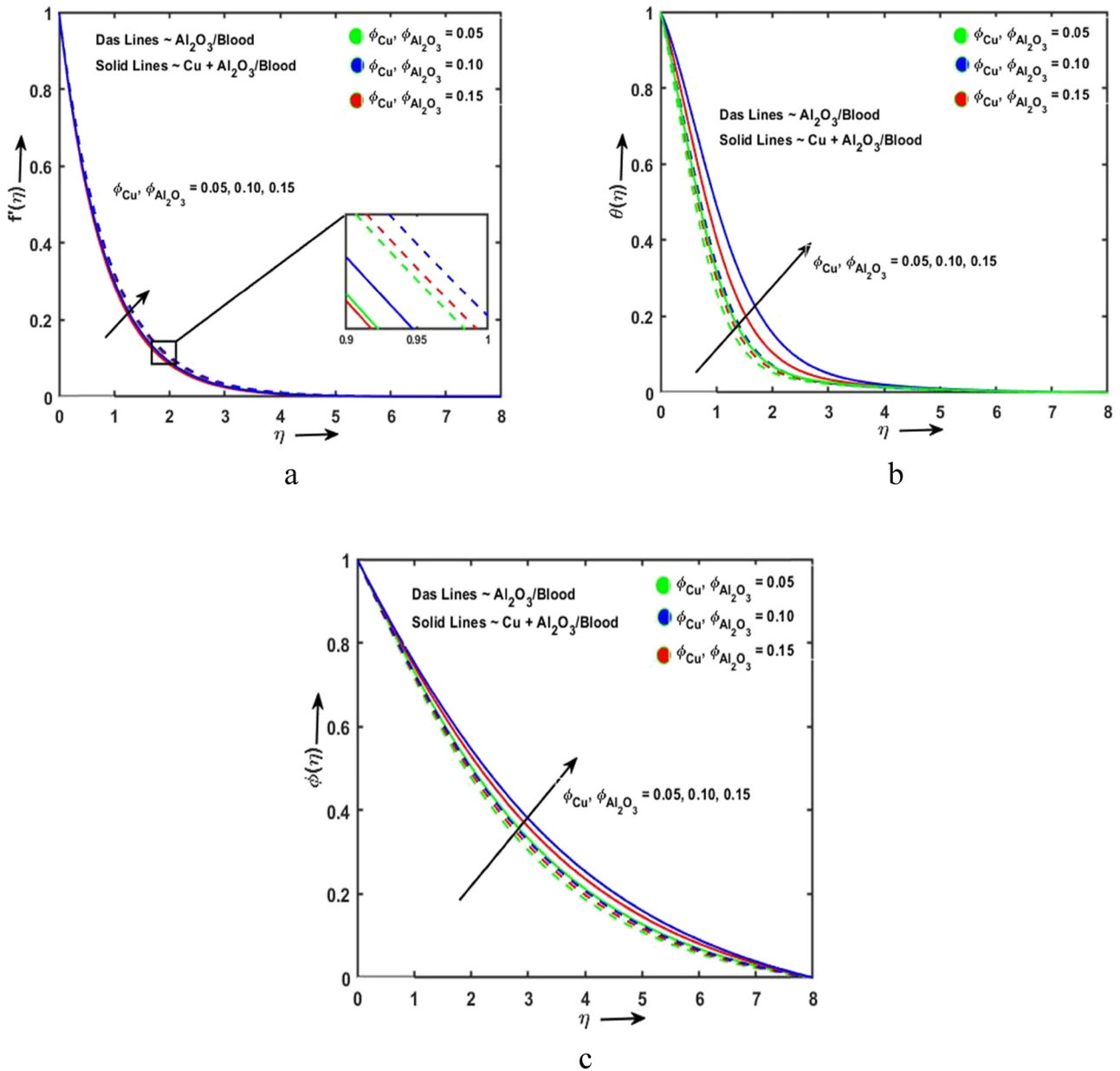


Figure 7: Variation outlines of volume fraction of  $nf$  and  $hnf$ . (a)  $f(\eta)$ , (b)  $\theta(\eta)$  and (c)  $\phi(\eta)$ .

Figure 8a and b illustrates the gain temperature impressions of Dufour and the heat source parameter. A concentration gradient causes an energy flux, which is what the Dufour number measures, *i.e.*, when the Dufour number grows, the energy flux also rises; therefore, temperature upsurges. On the other hand, the heat source is a producer of the heat, so temperature increases.

The effect of viscous dissipation is denoted by the Eckert number. It is a measurement that illustrates the relationship between enthalpy and kinetic energy. Physically, when the dissipation increases, the fluid thermal conductivity increases, contributing to a rise in the thermal boundary layer

thickness. Figure 9a shows the temperature increases with the upsurge Eckert parameter. The concentration declines  $\eta < 2.5$  while gaining  $\eta > 2.5$  (as shown in Figure 9b) for both  $nf$  and  $hnf$ . An increase in  $Ec$  has been shown to accelerate the thermal profile. The concentration distributions for the elevating values of  $Ec$  are shown in Figure 9b. A growing role of  $Ec$  seems to be the concentration field.

The temperature is improving (Figure 10a), and the concentration is declining (Figure 10b) for the upsurge radiation parameter. The reality that more energy is created by the radiation mechanism, for which the radiation parameter is raised, is reinforced physically.

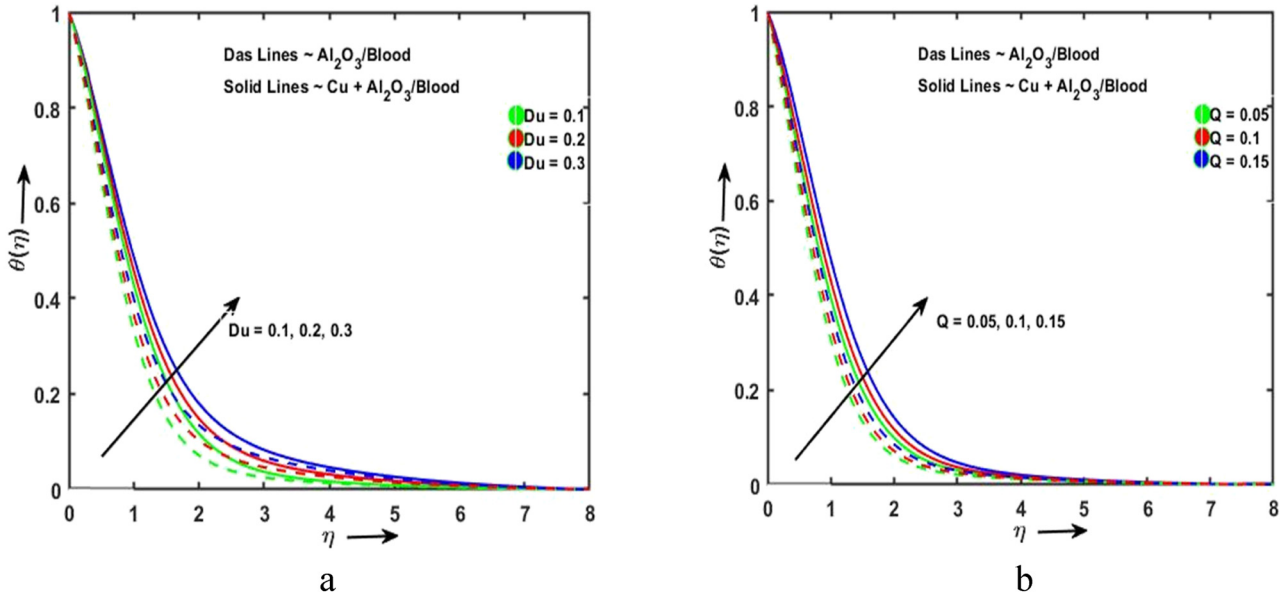


Figure 8: Temperature variances of (a)  $Du$  and (b)  $Q$ .

An increasing consequence of the Prandtl number on temperature is shown in Figure 11a for both nf and hnf. The arcs in this diagram show that a rise in  $Pr$  results in a reduction in the energy profile. The thermal conductivity reductions cause the decrease in the thermal outlines as  $Pr$  increases.

Figure 11a illustrates the growing temperature impression, and Figure 11b shows the falling concentration impression of upsurge Schmidt number for both nf and hnf. In reality, when  $Sc$  rises, the fluid molecular/mass diffusivity declines, which in go lowers the concentration of flowing fluid.

The temperature declines (Figure 12a), and concentration grows (Figure 12b) with a rising Soret impression for both nf and hnf. Temperature gradient impacted the concentration variation in the Soret phenomena. Therefore, more significant Soret numbers lead to more convective movement and, ultimately, higher concentrations.

Figure 13a and b depict the upsurge temperature and decline concentration impacts for the variable of thermal conductivity for both nf and hnf, respectively. It should be observed that when the variable thermal conductivity

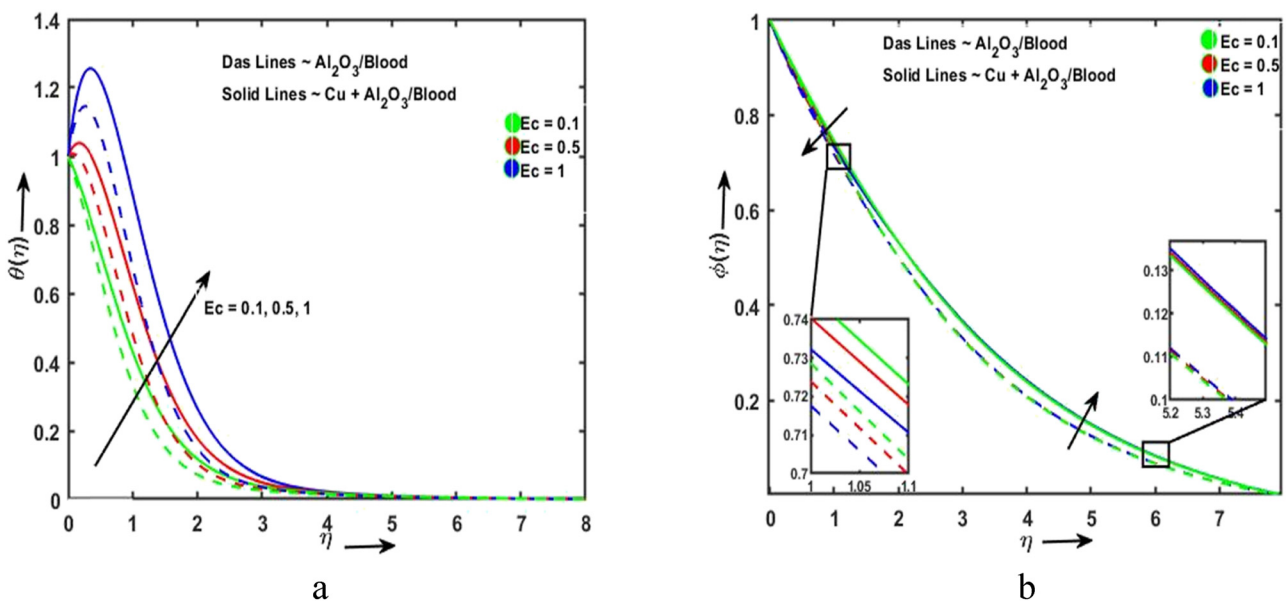


Figure 9: (a) Temperature and (b) concentration variances of  $Ec$ .



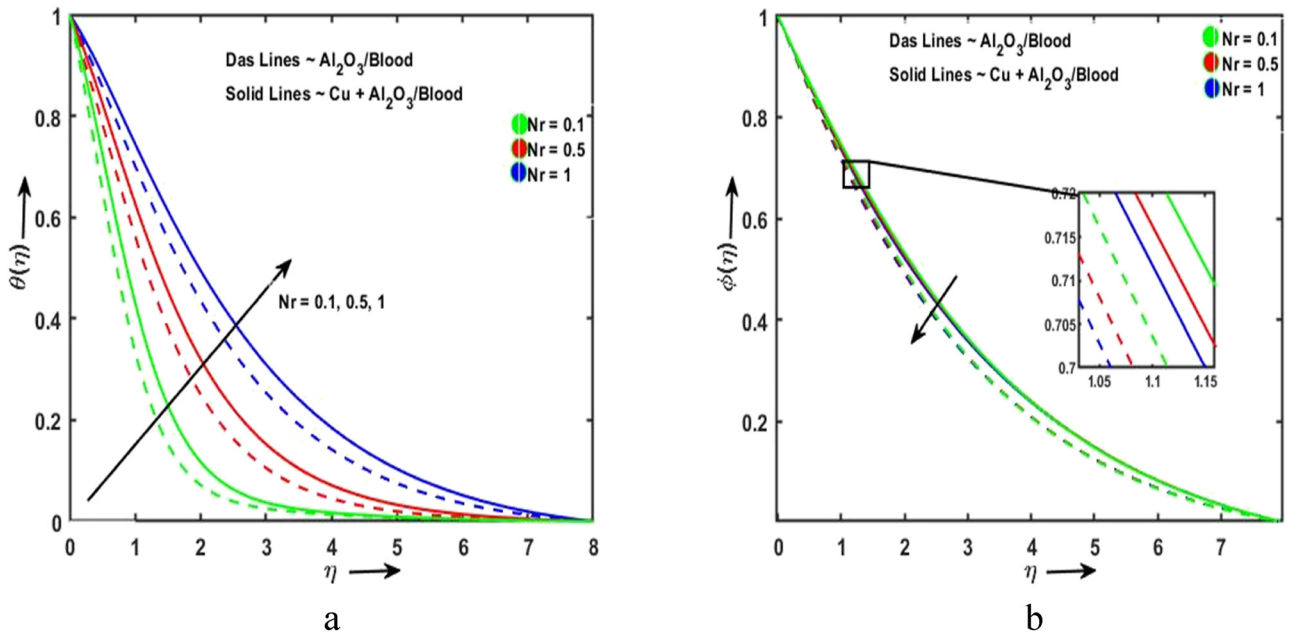


Figure 10: (a) Temperature and (b) concentration variances of  $Nr$ .

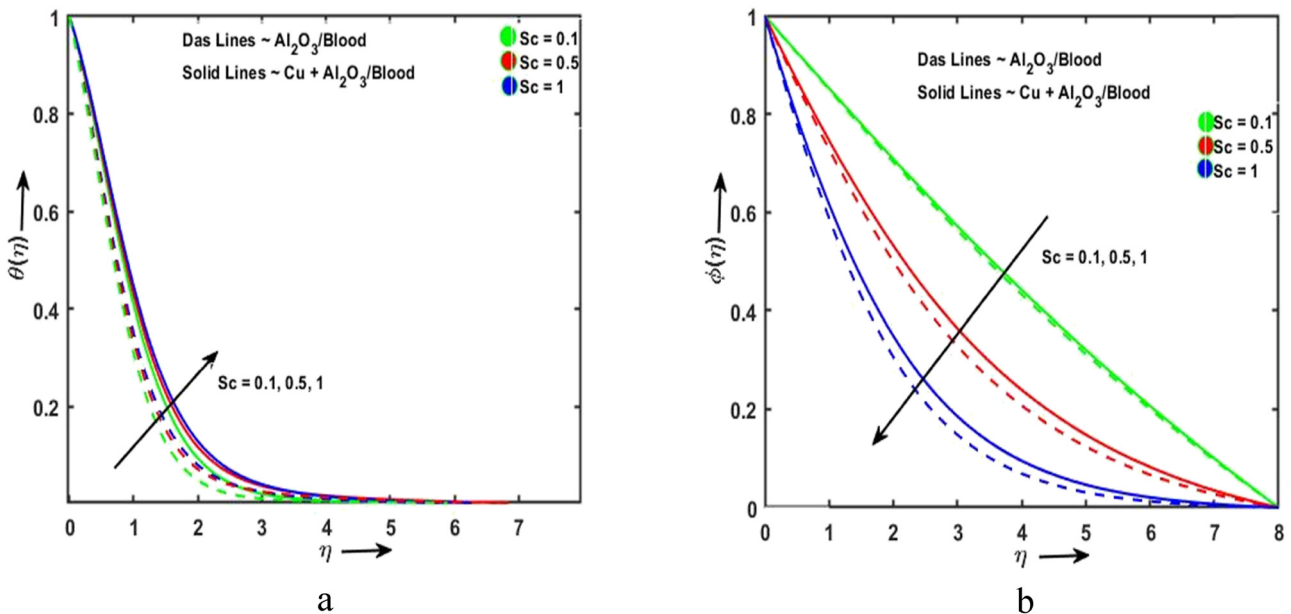


Figure 11: (a) Temperature and (b) concentration variances of  $Sc$ .

parameter rises, the temperature also tends to increase. This is caused by the thickening of the thermal boundary layer; its impact is more significant at the boundary layer and lessens as you go closer to the free stream.

Tables 5 and 6 express the rates of skin friction, heat, and mass transportation. Skin friction rate decays with magnetic, volume fractions of  $Cu$  and  $Al_2O_3$ , and permeability, while the opposite impression shows for Weissenberg

parameter and power law index. Nusselt number grows with Prandtl, Soret, and the volume fractions of  $Cu$  and  $Al_2O_3$ , while the opposite impact is seen for Eckert, heat source, radiation, Dufour, Schmidt, the variable of thermal conductance, and power law index. Sherwood number increases with Eckert, heat source, radiation, Dufour, Schmidt, the variable of thermal conductance, and volume fractions of  $Cu$  and  $Al_2O_3$ , while it decreases with Prandtl, Soret, and power law index.

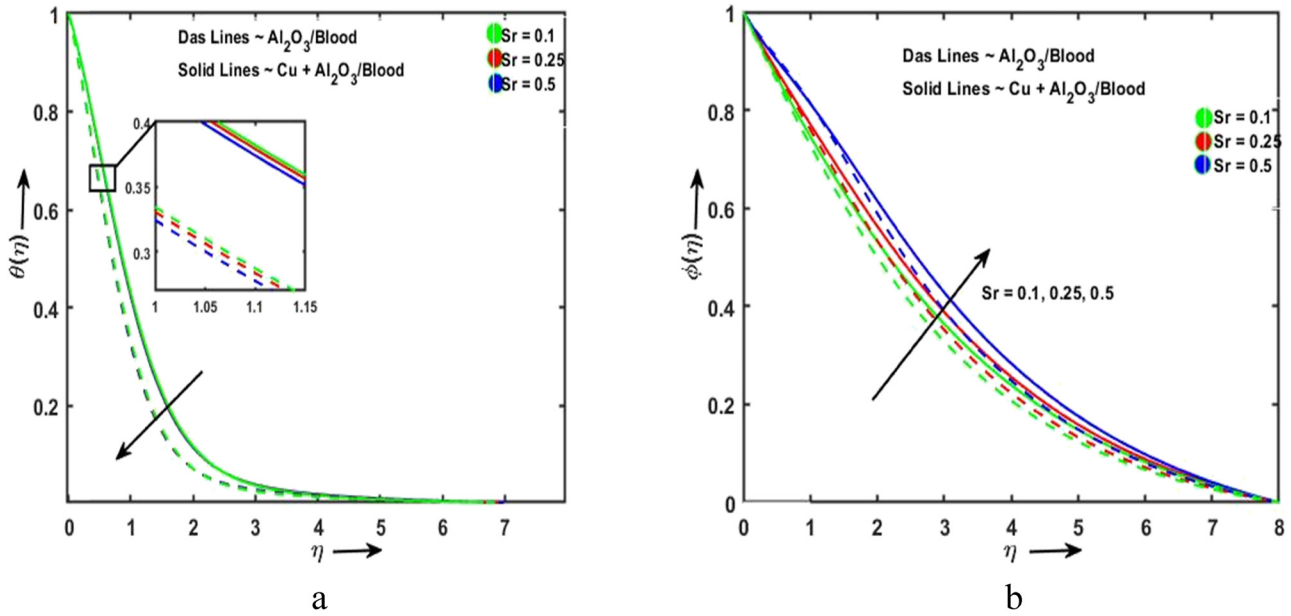


Figure 12: (a) Temperature and (b) concentration variances of Sr.

### 4 Conclusions

A two-dimensional steady nonlinear incompressible radiative tangent hyperbolic hybrid nanofluid flow over a porous extending along with the magnetic field, joule heating, viscous dissipation, heat source, and cross-diffusion impressions studied in existing research. We may expand this work in the future by utilizing other geometries, including

3D surfaces and Riga plates, as well as various kinds of nanomaterials with the base fluid. In addition, we consider the steady-to-unsteady problem. The following is a list of the experiment key findings:

- The skin friction rate declines with the magnetic and permeability impressions.
- Growing Prandtl increases Nusselt number, while the reverse impression is seen with Eckert, Dufour, and radiation.

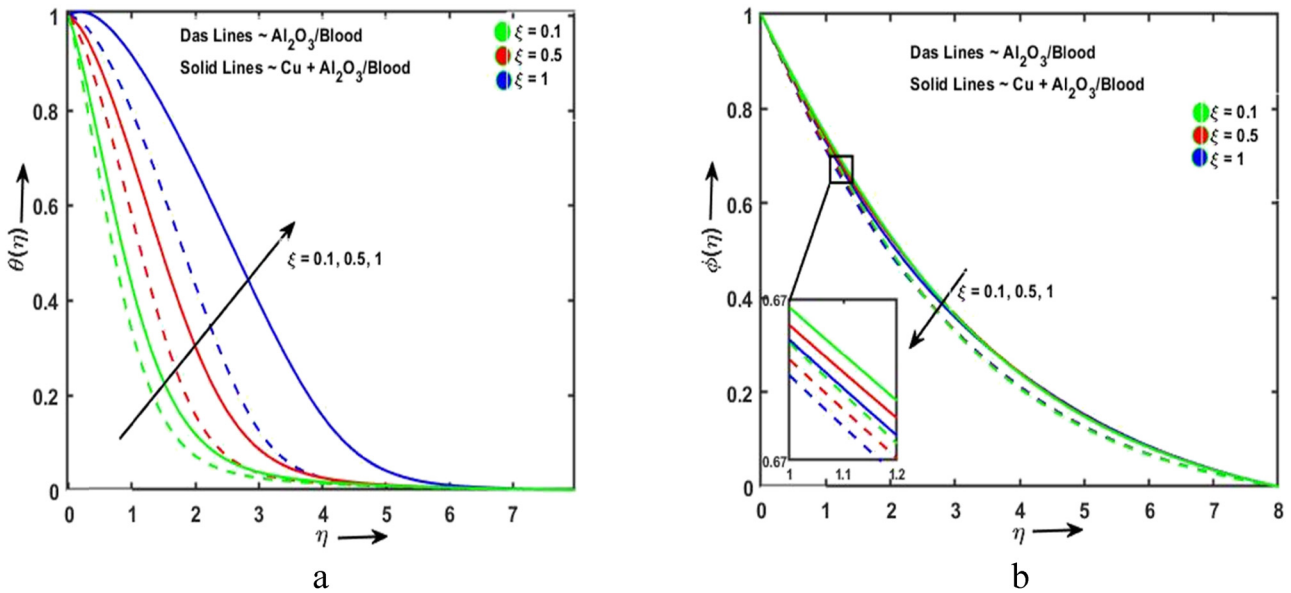


Figure 13: (a) Temperature and (b) concentration variances of  $\xi$ .

**Table 5:** The rates of skin-friction, Nusselt, and Sherwood with Mn, K, W, Pr, Ec, Q, and Nr when Sc = 0.5,  $\phi_{Cu} = 0.03$ ,  $\phi_{Al_2O_3} = 0.01$ , Du =  $\xi = Sr = n = 0.1$

Mn	K	W	Pr	Ec	Q	Nr	$Cf_x Re_x^{1/2}$		$Nu_x Re_x^{1/2}$		$Sh_x Re_x^{1/2}$	
							Al <sub>2</sub> O <sub>3</sub> /blood	Cu-Al <sub>2</sub> O <sub>3</sub> /blood	Al <sub>2</sub> O <sub>3</sub> /blood	Cu-Al <sub>2</sub> O <sub>3</sub> /blood	Al <sub>2</sub> O <sub>3</sub> /blood	Cu-Al <sub>2</sub> O <sub>3</sub> /blood
0.1							-1.518727323	-2.034439869	0.913483700	0.854196684	0.342362090	0.352582161
0.5	0.1	0.1	24	0.1	0.1	0.1	-1.768430863	-2.342184990	0.686440322	0.545480251	0.323699920	0.336523046
1							-2.037717519	-2.677253781	0.435904247	0.200677487	0.308704087	0.323850347
	0.1						-1.518727323	-2.034439869	0.913483700	0.854196684	0.342362090	0.352582161
	0.5						-1.764154213	-2.330158692	0.778232693	0.677930601	0.321423416	0.334357109
	1						-2.029368949	-2.653562760	0.625000555	0.475019722	0.303799785	0.318951436
		0.1					-1.518727323	-2.034439869	0.913483700	0.854196684	0.342362090	0.352582161
		1					-1.486264867	-1.988183489	0.904476306	0.842676581	0.339428284	0.349577886
		2					-1.446536957	-1.931175841	0.892671157	0.82750776	0.335856695	0.345908753
			2				-1.518727324	-2.034439869	0.537039455	0.462423840	0.352064296	0.360637534
			4				-1.518727323	-2.034439869	0.773357166	0.711275819	0.345886126	0.355339479
			6.8				-1.518727323	-2.034439869	0.913483700	0.854196684	0.342362090	0.352582161
				0.1			-1.518727323	-2.034439869	0.913483700	0.854196684	0.342362090	0.352582161
				0.5			-1.518727323	-2.034439870	-0.337925759	-1.060205382	0.378552765	0.395477368
				1			-1.518727322	-2.034439870	-2.072309392	-3.799577167	0.428803013	0.456988972
					0.05		-1.518727323	-2.034439869	1.051862218	1.035798236	0.338427065	0.348595624
					0.1		-1.518727323	-2.034439869	0.913483700	0.854196684	0.342362090	0.352582161
					0.15		-1.518727323	-2.034439870	0.757251826	0.642347944	0.346791449	0.357219344
						0.1	-1.518727323	-2.034439869	0.913483700	0.854196684	0.342362090	0.352582161
						0.5	-1.518727323	-2.034439869	0.827419319	0.801491203	0.350221111	0.357906888
						1	-1.518727323	-2.034439869	0.742097035	0.728033522	0.355658172	0.362077765

**Table 6:** The rates of skin friction, Nusselt, and Sherwood with Du, Sc, Sr,  $\xi$ , n,  $\phi_{Al_2O_3}$  and  $\phi_{Cu}$  when Mn = 0.5, K = W = Ec = Q = Nr = 0.1, Pr = 24

Du	Sc	Sr	$\xi$	n	$\phi_{Al_2O_3}$	$\phi_{Cu}$	$Cf_x Re_x^{1/2}$		$Nu_x Re_x^{1/2}$		$Sh_x Re_x^{1/2}$		
							Al <sub>2</sub> O <sub>3</sub> /blood	Cu-Al <sub>2</sub> O <sub>3</sub> /blood	Al <sub>2</sub> O <sub>3</sub> /blood	Cu-Al <sub>2</sub> O <sub>3</sub> /blood	Al <sub>2</sub> O <sub>3</sub> /blood	Cu-Al <sub>2</sub> O <sub>3</sub> /blood	
0.1							-1.518727323	-2.034439869	0.913483700	0.854196684	0.342362090	0.352582161	
0.2	0.5	0.1	0.1	0.1	0.01	0.03	-1.518727323	-2.034439869	0.844064382	0.779039847	0.344279584	0.354221877	
0.3							-1.518727323	-2.034439869	0.772432733	0.701636439	0.346259848	0.355910819	
		0.1					-1.518727323	-2.034439869	0.965239128	0.910800944	0.180224920	0.194430817	
		0.5					-1.518727323	-2.034439869	0.913483700	0.854196684	0.342362090	0.352582161	
		1					-1.518727323	-2.034439869	0.864786380	0.799817685	0.550629116	0.563117378	
			0.1				-1.518727323	-2.034439869	0.913483700	0.854196684	0.342362090	0.352582161	
			0.25				-1.518727323	-2.034439869	0.917932182	0.856720000	0.311547841	0.331916348	
			0.5				-1.518727323	-2.034439869	0.925364503	0.860854562	0.259481628	0.297214574	
				0.1			-1.518727323	-2.034439869	0.913483700	0.854196684	0.342362090	0.352582161	
				0.5			-1.518727324	-2.034439869	0.316681473	0.174117260	0.358635848	0.366861819	
				1			-1.518727323	-2.034439868	0.032468154	-0.191696210	0.365797830	0.374520528	
					0.1		-1.518727323	-2.034439869	0.913483700	0.854196684	0.342362090	0.352582161	
					0.4		-1.221562313	-1.634816788	0.837573044	0.752175253	0.309373251	0.320390537	
					0.6		-0.963648343	-1.286431580	0.708457012	0.565621380	0.279121881	0.291994418	
						0.009	0.02	-1.179776516	-1.429270257	0.864422507	0.843539169	0.318675753	0.319074286
						0.010	0.025	-1.339046942	-1.882579563	0.891121437	0.833345698	0.329556705	0.338493866
						0.010	0.03	-1.518727323	-2.429228233	0.913483700	0.795560466	0.342362090	0.365295232

- Sherwood number upsurge with Schmidt number and decays with Soret number.
- Temperature and concentration rise with the upsurge power law index, while the motion declines with the upsurge power law index.
- Temperature increases with the increasing variable of thermal conductance, while concentration declines with the growing variable of thermal conductivity.
- Many practical and scientific applications based on the dynamics of blood flow over a stretching sheet are expected in the future. The current study's findings could be used to numerous model investigations. The results of the current issue are also very intriguing for many fields of science and technology, such as lubricants, emulsions, cancer therapy, biofluids in biological polymer and tissue, drug transportation, nuclear fuel slurries, cancer tumor treatment, and bio-medical fluids.

**Acknowledgments:** The authors extend their appreciation to the Deanship of Research and Graduate Studies at King Khalid University for funding this work through Large Research Project under grant number RGP: 2/411/45.

**Funding information:** The Deanship of Research and Graduate Studies at King Khalid University for funding this work through Large Research Project under grant number RGP: 2/411/45.

**Author contributions:** All authors have accepted responsibility for the entire content of this manuscript and approved its submission.

**Conflict of interest:** The authors state no conflict of interest.

**Data availability statement:** The datasets generated and/or analyzed during the current study are available from the corresponding author on reasonable request.

## References

- [1] Abbas N, Nadeem S, Saleem A, Malik MY, Issakhov A, Alharbi FM. Models base study of inclined MHD of hybrid nanofluid flow over nonlinear stretching cylinder. *Chin J Phys.* 2021;69:109–17.
- [2] Ahmad F, Abdal S, Ayed H, Hussain S, Salim S, Almatroud AO. The improved thermal efficiency of Maxwell hybrid nanofluid comprising of graphene oxide plus silver/kerosene oil over stretching sheet. *Case Stud Therm Eng.* 2021;27:101257.
- [3] Riaz A, Ellahi R, Sait SM. Role of hybrid nanoparticles in thermal performance of peristaltic flow of Eyring–Powell fluid model. *J Therm Anal Calorim.* 2021;143:1021–35.
- [4] Aladdin NAL, Bachok N, Pop I. Cu–Al<sub>2</sub>O<sub>3</sub>/water hybrid nanofluid flow over a permeable moving surface in presence of hydromagnetic and suction effects. *Alex Eng J.* 2020;59(2):657–66.
- [5] Ali ZM, Ismail NZ, Ilias MR, Soid SK, Ishak A, Basir MFM, et al. Hyperbolic tangent fluid model for stagnation flow of hybrid nanofluid over a stretching sheet. *J Adv Res Fluid Mech Therm Sci.* 2023;107(1):87–101.
- [6] Atif SM, Hussain S, Sagheer M. Effect of viscous dissipation and Joule heating on MHD radiative tangent hyperbolic nanofluid with convective and slip conditions. *J Braz Soc Mech Sci Eng.* 2019;41:1–17.
- [7] Awais M, Kumam P, Ali A, Shah Z, Alrabaiah H. Impact of activation energy on hyperbolic tangent nanofluid with mixed convection rheology and entropy optimization. *Alex Eng J.* 2021;60(1):1123–35.
- [8] Devi SA, Devi SSU. Numerical investigation of hydromagnetic hybrid Cu–Al<sub>2</sub>O<sub>3</sub>/water nanofluid flow over a permeable stretching sheet with suction. *Int J Nonlinear Sci Numer Simul.* 2016;17(5):249–57.
- [9] Gul T, Khan A, Bilal M, Alreshidi NA, Mukhtar S, Shah Z, et al. Magnetic dipole impact on the hybrid nanofluid flow over an extending surface. *Sci Rep.* 2020;10(1):8474.
- [10] Devi SU, Devi SA. Heat transfer enhancement of Cu–Al<sub>2</sub>O<sub>3</sub>/water hybrid nanofluid flow over a stretching sheet. *J Niger Math Soc.* 2017;36(2):419–33.
- [11] Hafeez A, Khan M, Ahmed J, Ahmed A, Iqbal Z. Flow of Oldroyd-B fluid over a rotating disk through porous medium with Soret–Dufour effects. *Arab J Sci Eng.* 2020;45:5949–57.
- [12] Kasali KB, Tijani YO, Lawal MO, Lawal YT. Soret, Dufour and radiation effects of a viscoelastic fluid on an exponentially stretching surface using the Cattaneo–Christov heat flux model. *Multidiscip Model Mater Struct* 16(6):1577–94.
- [13] Noreen S, Riaz A, Lu D. Soret–Dufour effects in electroosmotic biorheological flow of Jeffrey fluid. *Heat Transf.* 2020;49(4):2355–74.
- [14] Gautam AK, Verma AK, Bhattacharyya K, Banerjee A. Soret and dufour effects on MHD boundary layer flow of non-Newtonian Carreau fluid with mixed convective heat and mass transfer over a moving vertical plate. *Pramana.* 2020;94(1):1–10.
- [15] Salleh SNA, Bachok N, Md. Arifin N, Md. Ali F. Influence of Soret and Dufour on forced convection flow towards a moving thin needle considering Buongiorno's nanofluid model. *Alex Eng J.* 2020;59(5):3897–906.
- [16] Hanif H, Shafie S, Chamkha A. Effect of Ohmic heating on magnetohydrodynamic flow with variable pressure gradient: a computational approach. *Waves Random Complex Media.* 2022;1–16. doi: 10.1080/17455030.2022.2141916.
- [17] Hanif H, Shafie S, Roslan R, Ali A. Collision of hybrid nanomaterials in an upper-convected Maxwell nanofluid: A theoretical approach. *J King Saud Univ-Sci.* 2023;35(1):102389.
- [18] Izady M, Dinarvand S, Pop I, Chamkha AJ. Flow of aqueous Fe<sub>2</sub>O<sub>3</sub>–CuO hybrid nanofluid over a permeable stretching/shrinking wedge: A development on Falkner–Skan problem. *Chin J Phys.* 2021;74:406–20.
- [19] Jamshed W, Nisar KS, Ibrahim RW, Shahzad F, Eid MR. Thermal expansion optimization in solar aircraft using tangent hyperbolic hybrid nanofluid: A solar thermal application. *J Mater Res Technol.* 2021;14:985–1006.
- [20] Jamshed W, Prakash M, Devi S, Ibrahim RW, Shahzad F, Nisar KS, et al. A brief comparative examination of tangent hyperbolic hybrid

- nanofluid through a extending surface: numerical Keller–Box scheme. *Sci Rep.* 2021;11:24032
- [21] Khan Y. Magnetohydrodynamic flow of linear visco-elastic fluid model above a shrinking/stretching sheet: A series solution. *Sci Iran.* 2017;24(5):2466–72.
- [22] Khan Y. Two-dimensional boundary layer flow of chemical reaction MHD fluid over a shrinking sheet with suction and injection. *J Aerosp Eng.* 2014;27(5):04014019.
- [23] Khan Y, Mohyud-Din ST. Coupling of He's polynomials and Laplace transformation for MHD viscous flow over a stretching sheet. *Int J Nonlinear Sci Numer Simul.* 2010;11(12):1103–8.
- [24] Khan Y, Wu Q, Faraz N, Yildirim A. The effects of variable viscosity and thermal conductivity on a thin film flow over a shrinking/ stretching sheet. *Comput Maths Appl.* 2011;61(11):3391–9.
- [25] Loganathan K, Alessa N, Tamilvanan K, Alshammari FS. Significances of Darcy–Forchheimer porous medium in third-grade nanofluid flow with entropy features. *Eur Phys J Spec Top.* 2021;230:1293–305.
- [26] Madhukesh JK, Kumar RN, Gowda RP, Prasannakumara BC, Ramesh GK, Khan MI, et al. Numerical simulation of AA7072-AA7075/water-based hybrid nanofluid flow over a curved stretching sheet with Newtonian heating: A non-Fourier heat flux model approach. *J Mol Liq.* 2021;335:116103.
- [27] Nadeem M, Siddique I, Riaz Z, Makhdoum BM, Zulqarnain RM, Sallah M. Numerical study of unsteady tangent hyperbolic fuzzy hybrid nanofluid over an exponentially stretching surface. *Sci Rep.* 2023;13(1):15551.
- [28] Shoaib M, Raja MAZ, Sabir MT, Islam S, Shah Z, Kumam P, et al. Numerical investigation for rotating flow of MHD hybrid nanofluid with thermal radiation over a stretching sheet. *Sci Rep.* 2020;10(1):18533.
- [29] Suresh S, Venkitaraj KP, Selvakumar P, Chandrasekar M. Effect of Al<sub>2</sub>O<sub>3</sub>–Cu/water hybrid nanofluid in heat transfer. *Exp Therm Fluid Sci.* 2012;38:54–60.
- [30] Ullah Z, Zaman G, Ishak A. Magnetohydrodynamic tangent hyperbolic fluid flow past a stretching sheet. *Chin J Phys.* 2020;66:258–68.
- [31] Venkateswarlu B, Satya Narayana PV. Cu-Al<sub>2</sub>O<sub>3</sub>/H<sub>2</sub>O hybrid nanofluid flow past a porous stretching sheet due to temperature-dependent viscosity and viscous dissipation. *Heat Transf.* 2021;50(1):432–49.